SCIENCE CHINA
Information Sciences

Supplementary information

Appendix A. Fabrication and design of devices

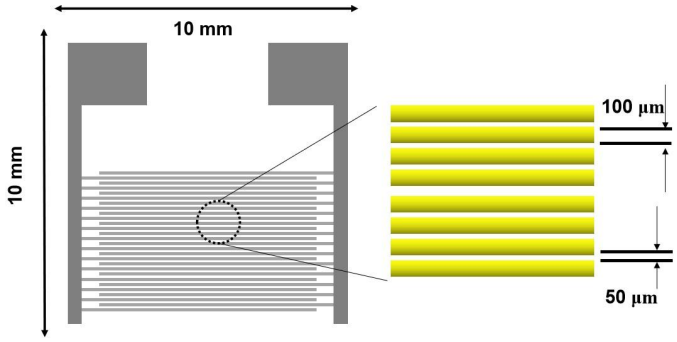

Fig.S1.Substrate parameters

Substrate parameters are shown in Fig.S1. The substrate material is alumina ceramic. The dimensions of the device are 10 mm × 10 mm with a line spacing of 50 μm and a line width of 100 μm. The electrode length is 7.7 mm and the number of fork-finger electrodes is 30. The metal layer structure is Ti/Cu/Ni/Au with thicknesses of 0.1 μm, 5 μm, 4 μm, and 1 μm respectively. The $SnSe_2$ material layers are processed on this substrate by magnetron sputtering methods.

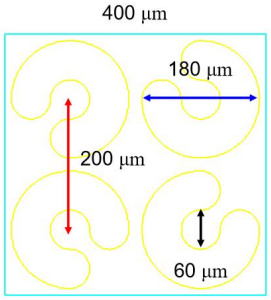

Fig.S2.Parameters of the Au ring array unit

Parameters of the Au ring array unit are shown in Fig.2S. The inner diameter of 60 μm and outer diameter of 180 μm of each ring is designed, with the space between two rings of 200 μm. Each ring was designed with a gap at 1/4 of the top left ring, with the four-ring gaps in the clockwise direction being the bottom left, top left, top right, and bottom right respectively. The four rings are a unit with dimensions of 400 μm × 400 μm.

The details of device processing are described as follows: at first, the air pressure was reduced to 9×10^{-4} Pa and injected argon into the cavity. $SnSe_2$ target is coated using RF drive mode. The argon flow rate of 50 SCCM, power of 100 W, and duration time of 220 secs were set. After that, with a split ring array mask covered on the $SnSe_2$ film, the Au-SRA were coated. The Au target is coated using DC drive mode. The argon flow rate, current, and duration time of 15 SCCM, 0.2 A, and 90 secs were set. Finally, we also

deposited SiO_2 on the device for 30 secs to isolate the device from the air and improve its stability.

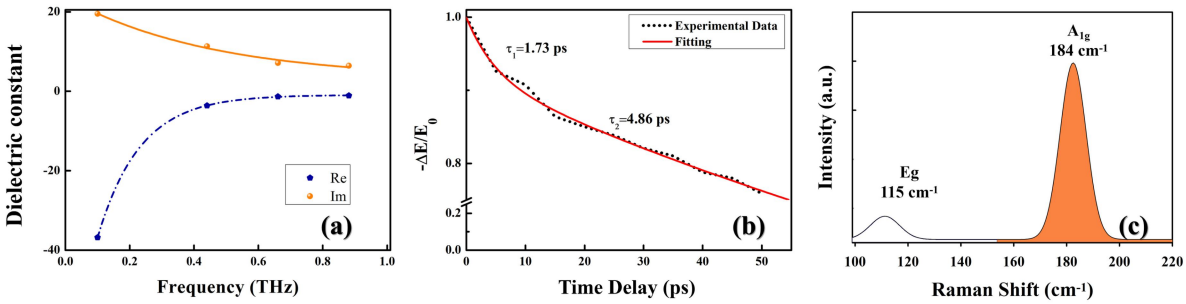

Fig.S3. Characterizations of the device. (a) The complex dielectric constant dispersion of $SnSe_2$ film. (b) Optical pump induced THz relative transmission change ($\Delta E/E_0$) as a function of pump delay for $SnSe_2$ film. (c) Raman spectra.

Fig.S3a shows the complex dielectric constant dispersion of $SnSe_2$ film in the THz spectrum. We used the following equation to demonstrate the dielectric constant of the ultrathin film[1]:

$$\varepsilon(\omega)=\frac{i(n+1)c}{\omega d}\frac{1-T/T_0}{T/T_0} \tag{1}$$

n is the refractive index, d is the film thickness, c is the speed of light in a vacuum and T/T_0 is the complex transmittance. Drude model was used to fit the complex dielectric constant [1]:

$$\varepsilon(\omega)=\varepsilon_\infty-\frac{\omega_p^2}{\omega(\omega+i\gamma)} \tag{2}$$

Where ε_∞, ω_p, and γ are the dielectric constant for high frequency, plasma frequency, and damping constant, respectively. The charge carrier dynamic of $SnSe_2$ film was tested by the optical-induced probe time delay recorded. Fig.S3b shows the change in the maximum THz signal ΔE normalized by probe field E. The fast decay τ_1 is caused by the hot carriers' energy relaxation until thermal equilibrium, while the slow decay τ_2 demonstrates the lifetime of carriers. The carrier dynamic was fitted by the biexponential decay function [2]:

$$-\frac{\Delta E}{E_0}=A_1\exp\left(-\frac{\tau}{t_1}\right)+A_2\exp\left(-\frac{\tau}{t_2}\right) \tag{3}$$

The fast time of 1.73 ps and slow time of 4.86 ps for the $SnSe_2$ film could be obtained, respectively. The Raman spectrometer used with 532 nm excitation is shown in Fig.S3c. The two peaks are the in-plane shear modes Eg at 115 cm^{-1} and out-of-plane breathing modes A_{1g} at 184 cm^{-1}, respectively[3,4].

Appendix B. Experimental process

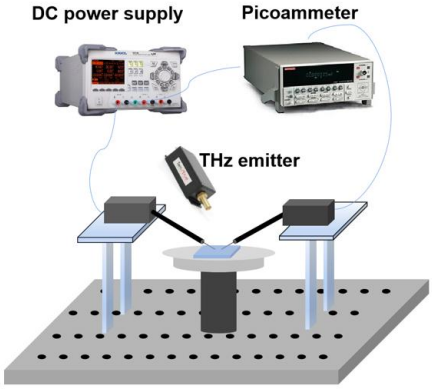

Fig.S4.Schematic diagram of the experimental setup

We use a light-dark current comparison method based on light current excitation to characterize the detection capability of the device (including I-V curve, total noise v_n, response R_V, NEP, D^*, etc.). The detection setup is shown in Fig.S4. The terahertz detector is placed in the center of the probe platform, and two tungsten probes (needle tip of 1μm) are used to contact the metal electrodes of the device and are connected in series with the DC power supply and the picoammeter. The terahertz avalanche diodes are used as terahertz sources, and the I-V curves recorded by the picoammeter (keithley 6485). Our incident wavelength 0.1 THz corresponds to 3 mm and 0.28 THz corresponds to 1.07 mm diffraction-limited area $S_\lambda = \lambda^2/4$[5], so 2.25 mm^2 and 0.25 mm^2 respectively. The total area of our device was larger than the diffraction-limited area.

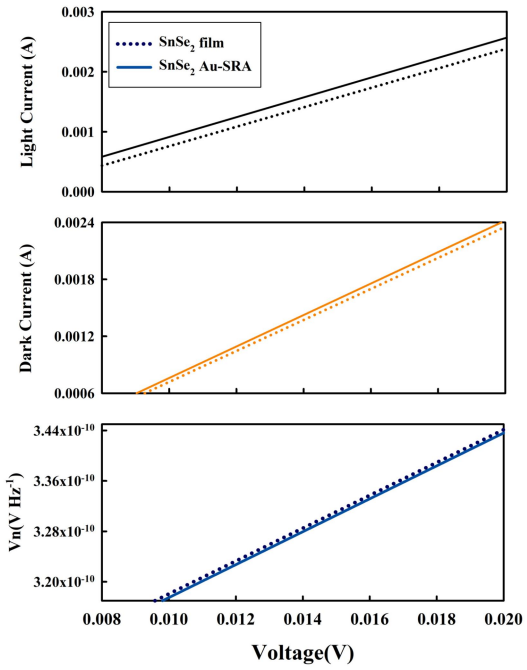

Fig.S5 Light current, dark current and Vn of the $SnSe_2$ film (as reference) and $SnSe_2$ Au-SRA at 0.28 THz

Fig.S5 shows the dark current and noise characterization. In the dark Ampere-Volt date, a rather good ohmic character of the $SnSe_2$ film (as reference) and $SnSe_2$ Au-SRA could be obtained. The $SnSe_2$ Au-SRA

and reference $SnSe_2$ film exhibit a remarkable difference in the light current level, due to the strong effect of the Au-SRA structure. The total noise (V_n) could be expressed by Eq.4. V_t is the thermal Johnson–Nyquist noise and V_b is the dark current shot noise [6]:

$$v_n = \sqrt{v_t^2 + v_b^2} = \sqrt{4k_B Tr + 2qI_d r^2} \tag{4}$$

Here, k_B, T, r, q, and I_d are Boltzmann's constant, detector's absolute temperature, resistance value, elementary charge, and dark current, respectively. The increasing V_n with the increased bias main caused by the increasing V_b. For the THz detectors, the performance of photoresponsivity (R_V), noise equivalent power (NEP), and detectivity (D^*), which are used to evaluate the photoelectrical conversion capability, could be expressed as Eq.5 [7]. V, P, and S are photovoltage, THz power, and effective detection area. V_n is the noise voltage (in Eq.4).

$$R_v = V / P \text{ , } NEP = V_n / R_A \text{ , } D^* = \sqrt{S} / NEP \tag{5}$$

Appendix C. Simulation

The THz field distributions on the device surface for 6G communication frequencies are shown in Fig.S6. The device exhibits a pronounced localization effect of the terahertz field in several typical 6G communication frequencies. Furthermore, in the range of 0.1-0.3 THz, the localization effect caused by the outer ring of the resonant ring decreases. For the inner ring, the localization effect increases with increasing frequency at the same time. Combining these two effects, the localization effect for THz waves gradually increases, i.e. the device has a stronger localization effect at 0.28 THz than 0.1 THz. Simulation results are consistent with experiments. In summary, our detector has great potential to be used in several typical 6G communication bands (0.1-0.3 THz).

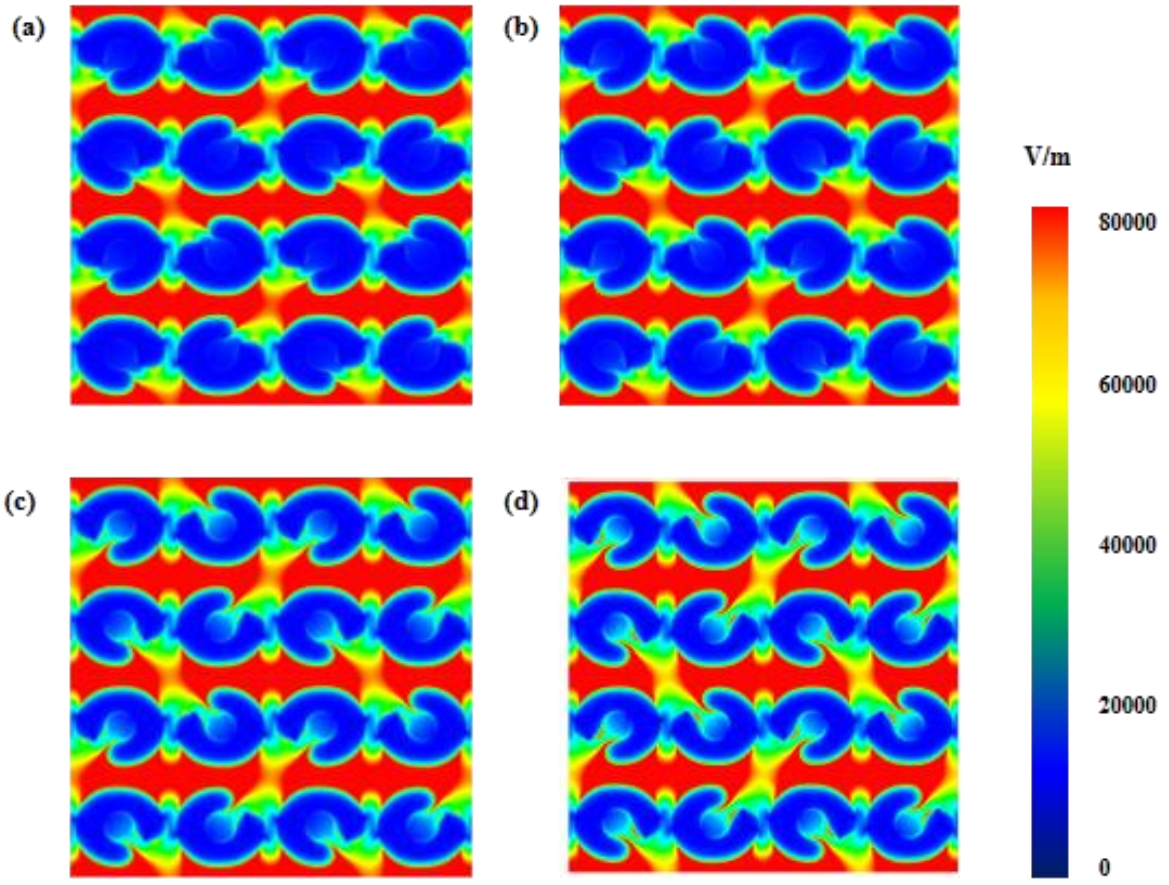

Fig.S6. THz field distribution on the device surface for 6G communication frequencies. (a) 0.1 THz, (b) 0.12 THz, (c) 0.22 THz, (d) 0.28 THz.

Appendix D. Comparison with other detectors

Tab.S1. Various types of THz detectors performances for different frequency

Material type	Responsivity (V/W)	NEP ($pW/Hz^{1/2}$)	bias(V)	Frequency (THz)	Ref
$TaSe_2$	27	100	0.08	0.12	8
BP	0.03	70000	4	0.298	9
TaS_2	96	-	0.72	3.11	10
	120	-		2.52	
	40	-		1.84	
bilayer graphene	30	51	1.4	0.33	11
hBN-BP-hBN	1.7	-	15	0.294	12
	0.3	100		0.295	
	0.2	-		0.593	
	0.9	-		0.627	
InSb	26000	0.02	1	0.171	7
$PtTe_2$	1400	10	0.1	0.12	13
$PdTe_2$	1.3×10^{-8}	2	0.1	0.12	14
MoS_2	76.56	-	20	2.52	15
Bi_2O_2Se	27000	0.2	0.5	0.17	16
$SnSe_2$	170	~10	0.1	0.12	17
Golay cell (Commercial)	1×10^5	140	-	0.03-20	18
Bolometer (Commercial)	2.4×10^5 (4.2K)	0.25 (4.2K)	-	0.15-20	19
graphene	1800	1000	0.2	0.3	20
SiGe	***6121***	***21***	***0.2***	***0.315***	21
lossy silicon	***2100***	***360***	***1.2***	***0.28***	22
bilayer graphene	4500 V/W (10 K)	**0.2** (10 K)	**2.6 V**	**0.13**	23
$SnSe_2$	***3073***	***0.1***	***0.02***	***0.28***	***This***
Au-SRA	***414***	***0.68***	***0.02***	***0.1***	***work***

The main technical performance of THz detectors based on different materials in recent years has been shown in Tab.S1. It can be seen that the $SnSe_2$ split-ring array detector combines the function of a split-ring array coupled with THz waves showing a good detection result for 6G communication frequency at 0.28 THz. Taking into account the lower operating voltage and the *NEP*, responsivity parameters, $SnSe_2$ split-ring array detector achieve results that are similar to those of the InSb detector[7], the best detector currently available, at a very low bias (1/50). Besides, if the operating voltage is further increased, the

detector performance will show even better characteristics. In addition, considering the large area uniformity of the $SnSe_2$ detector. It also has the potential to be further cut into micron-scale detector arrays for THz precision imaging of large area targets. In summary, the $SnSe_2$ Au-SRA detector proposed in our work has strong applications in 6G communications.

References

1. Yokota K, Takeda J, Dang C, et al. Surface metallic states in ultrathin Bi(001) films studied with terahertz time-domain spectroscopy. Appl.Phys.Lett., 2012, 100:251605.
2. Song Q, Chai L, Chen J Q, et al. Optically Tuned Wide-band Terahertz Modulation, Charge Carrier Dynamics and Photoconductivity of Femtosecond Laser Ablated Titanium Disulfide Nanosheet Devices. IEEE J.Sel.Top.Quant., 2021, 27(3):3500106.
3. Xiao P, Angel E C, Chaitoglou S, et al. Anisotropic Thermal Conductivity of Crystalline Layered $SnSe_2$. Nano Lett., 2021, 21:9172-9179.
4. Padha N and Kumar S. A two-step method to obtain the 2D layers of $SnSe_2$ single phase and study its physical characteristics for photovoltaic and photo-converter devices. Appl.Phys.A-Mater., 2021, 127:877.
5. M S Vitiello, D Coquillat, L Viti, et al. Room-Temperature Terahertz Detectors Based on Semiconductor Nanowire Field-Effect Transistors. Nano Lett., 2012, 12: 96-101.
6. Qiu Q X, Huang Z M. Photodetectors of 2D Materials from Ultraviolet to Terahertz Waves. Adv Mater., Mar., 2021, 33:2008126.
7. Tong J C, Suo F, Zhang T N, et al. Plasmonic semiconductor nanogroove array enhanced broad spectral band millimetre and terahertz wave detection. Light-Sci Appl., 2021, 10:58.
8. Wang J, Guo C, Guo W L, et al. Tunable 2H-$TaSe_2$ room-temperature terahertz photodetector. Chin. Phys. B., 2019, 28: 046802.
9. Viti L, Hu J, Coquillat D, et al. Black Phosphorus Terahertz Photodetectors. Adv. Mater., 2015, 27:5567-5572.
10. Wu D, Ma YC, Niu Y Y, et al. Ultrabroadband photosensitivity from visible toterahertz at room temperature. Sci.Adv., 2018, 4: eaao3057.
11. Qin H, Sun J D, Liang S X, et al. Room-temperature, low-impedance and high-sensitivity terahertz direct detector based on bilayer graphene field-effect transistor. Carbon, 2017, 116:760-765.
12. Viti L, Hu J, Coquillat D, et al. Heterostructured hBN-BP-hBN Nanodetectors at Terahertz Frequencies. Adv.Mater., 2016, 28:7390-7396.
13. Xu H, Guo C, Zhang J Z, et al. $PtTe_2$-Based Type-II Dirac Semimetal and Its van der Waals Heterostructure for Sensitive Room Temperature Terahertz Photodetection. Small, 2019, 15:1903362.
14. Guo C, Hu Y B, Chen G, et al. Anisotropic ultrasensitive $PdTe_2$-based phototransistor for room-temperature long-wavelength detection. Sci. Adv., 2020, 6:eabb6500.
15. Xie Y, Liang F, Chi S M, et al. Defect engineering of MoS_2 for room-temperature terahertz photodetection. ACS Appl.Mater.Interfaces., 2020, 12: 7351-7357.

16. Chen Y F, Ma W L, Tan C W, et al. Broadband Bi_2O_2Se photodetectors from infrared to terahertz. Adv. Funct. Mater., 2021, 31:2009554.
17. Guo C, Guo W L, Xu H, et al. Ultrasensitive ambient-stable $SnSe_2$-based broadband photodetectors for room-temperature IR/THz energy conversion and imaging. 2D Mater., 2020, 7(3):035026.
18. http://www.eachwave.com/Product/054637111.html(2019-06-14)[ACCESS 2022-4-22].
19. http://www.eachwave.com/Product/456031513.html(2019-06-14)[ACCESS 2022-4-22].
20. Yang X X, Vorobiev A, Jeppson K, et al. Describing Broadband Terahertz Response of Graphene FET Detectors by a Classical Model. IEEE T.THz. Sci. Techn., 2019, 10:158-165.
21. Yoon D, Kim J, Yun J, et al. 300-GHz direct and heterodyne active imagers based on 0.13-μm SiGe HBT technology. IEEE Trans. THz Sci. Technol., 2017, 7:536-545.
22. Han R, Zhang Y, Coquillat D, et al. A 280-GHz Schottky diode detector in 130-nm digital CMOS. IEEE J. Solid-State Circuits, 2011, 46: 2602-2612.
23. Gayduchenko I, Xu S G, Alymov G, et al. Tunnel field-effect transistors for sensitive terahertz detection. Nat. Commun., 2021, 12:543.